Check for
updates

A Gradient Smoothing Technique-Based S-FEM for Simulating the Full Impacts of Anomalies on Seepage Solutions and its Application in Multi-Parameter Seepage Inversion

Yi Lei[1] · Qianwei Dai[2,3] · Bin Zhang[2,3] · Chongyang Kong[2,3] · Junsheng Yang[1]

Abstract

Searching for the precise solution of the free surface has remained the main bottleneck in analyzing the unconfined seepage problem for earth-rock dams. This paper proposes an approach to solve classic earth-rock dams using the smoothed finite element method (S-FEM). To overcome the problems of complex calculation and accuracy loss caused by integrating the area of intersecting elements in saturated seepage, this paper optimizes the shape function calculation by reducing the area integral to a line integral along the elements. To achieve a balance between efficiency and accuracy, we investigated the distinct effects of various smooth elements on computational efficiency, which included computation time and iteration times. Moreover, we first explored the extensive effect of seepage anomalies and their positional changes on hydrological state variables, including head, free surface, overflow point, seepage velocity, and fluid pressure. This exploration presented could provide a potential for developing multi-parameter seepage inversion and serve as constraints for hydro-geophysical inversion.

Keywords Groundwater flow · Heterogeneity · Seepage analysis · Free surface searching · Smoothed finite element · Hydrological state variables

1 Introduction

Unconfined seepage analysis is of great significance for many applications such as geotechnical engineering, groundwater hydrology, hydro-geophysics and the stability of high earth-rock dams (Zhang et al. 2017; Yang et al. 2019; Sharma et al. 2021). Seepage flow beneath a hydraulic structure is formed by the hydraulic head difference between the upstream and downstream sides (Nafiseh et al. 2018). Excessive seepage or pore pressure

✉ Bin Zhang
 geophysic@csu.edu.cn

[1] School of Civil Engineering, Central South University, Changsha, China

[2] School of Geosciences and Info-Physics, Central South University, Changsha, China

[3] Key Laboratory of Metallogenic Prediction of Nonferrous Metals and Geological Environment Monitoring, Ministry of Education, Changsha, China

could have a great potential to cause serious instability of high earth-rock dams (Farzin et al. 2020; Rehamnia et al. 2020). Determining the precise position and accurate shape of the free surface remains a challenging task in the analysis of unconfined seepage. Its position and shape are influenced by various factors throughout the entire process of solving saturated seepage problems. In this sense, the unconfined seepage analysis is essentially considered a multivariable domain problem with strong nonlinearity and time-varying characteristics (Zheng et al. 2005; Butera et al. 2020).

Numerous numerical approaches have been employed to analyze unconfined seepage, including the moving-mesh method, meshless method, and the fixed-mesh method. By repositioning the boundary elements to alter the solution domain, the moving-mesh method has been proven to be one of the most preferred approaches for solving problems involving varying domains (Darbandi et al. 2007; Dai et al. 2019; Sharma et al. 2021). However, the meshing process of moving-mesh methods is reported to be time-consuming because it involves remeshing the model every iteration to address variable domain problems (Dou et al. 2017). In addition, mesh distortions may be caused by remeshing during the iteration process, especially in the presence of non-uniform media or geometric distortions, which can result in a reduction in accuracy that limits its applicability. To address the heterogeneity issue of seepage, other meshless methods have also been suggested, such as the natural element method (NEM) (Shahrokhabadi and Toufigh 2013), the numerical manifold method (NMM) (Zheng et al. 2015), and the moving Kriging meshless method (Zhang et al. 2017). However, due to the typical use of local interpolations in the meshless method for solution approximation, dealing with intricate boundaries and complex models may potentially lead to numerical stability concerns. In fact, the meshless method's unique characteristics necessitate additional steps when obtaining hydrological state variables during post-processing compared to conventional finite element method (FEM) and finite difference method (FDM).

Remeshing can be avoided by using the fixed-mesh method, which reduces the dependence on the meshing. Proper formulation of boundary intersecting elements (BIE) is a crucial issue with the fixed-mesh method, since the BIE will be divided into different shapes when free surface changing continuously during the whole iterative process. And correspondingly, the synthesis of the stiffness matrix through area integration in the traditional FEM becomes more complicated. To address this issue, the residual flow method and variational inequality methods have been introduced, which have significantly improved the fixed-mesh method (Desai and Li 1983; Zheng et al. 2005; Daneshmand and Kazemzadeh-Parsi 2009). The unit decomposition techniques such as numerical manifold method (Jiang et al. 2010; Zheng et al. 2015) and scaled boundary finite element method (Bazyar and Talebi 2015; Johari and Heydari 2018) have also gained attention in the analysis of variable domain problems. In the applications of unconfined seepage analysis, however, imposing an accurate essential boundary or medium boundary conditions is infeasible in the course of forming the shape functions. Because the shape function in unit decomposition methods does not have the interpolation attribute like the finite element shape function, as evidenced by the delta interpolation strategy.

By using the gradient smoothing technique (GST) to reduce the dimension of the surface integral into the line integral along the boundaries, the smoothed finite element method (S-FEM) has been proposed and widely used in various engineering applications (Liu et al. 2007, 2009; He et al. 2011; Xue et al. 2013). With the assistance of the dimension reduction technique for surface integration, this method eliminates the significant influence of BIE shape on the accuracy and efficiency of the integral solution. For the standard cell-based smoothed finite element method (CS-FEM), each smoothed subdomain involves field nodes, smooth nodes (located at the edge center) and Gaussian points, preserving the FEM meshing

strategy while making minor modifications to the current finite element code. Theoretically, bilinear Q4 elements can be subdivided into infinite quadrilateral smoothing cells (SC), which means that more smoothed elements could represent more accurate solutions. But as Liu et al. (2009) pointed out that such subdivision is not generally necessary nor even preferable, a fundamental division of the element into four or less SC is one of the desirable choices for solid mechanics problems. By utilizing this feature of CS-FEM, Kazemzadeh-Parsi and Daneshmand (2012, 2013) analyzed unconfined seepage and computed the element matrices via GST without having to remesh. However, the study focused on analyzing the impact of inhomogeneous medium model on the distribution of free surface, while not involving the details of the intimate correlation among smoothing cells or the specific impact of anomalies and auxiliary structures on the distribution of hydrological state variables, which could be very beneficial for practical engineering design.

Within this context, we first used classical models to investigate the specific impact of different SCs on computational efficiency, including computation time and iteration counts. This investigation could help pinpoint the optimal quantity of SC that achieves a trade-off between efficiency and accuracy. At the same time, the validity of the method was evaluated through classical model experiments. The testing model was specifically designed to explore the impact of factors like the location of anomalies and the magnitude of permeability on hydrological state variables, which involve the free surface, overflow points, seepage velocity, and fluid pressure. The findings enabled us to gain a deeper understanding of how inhomogeneity impacts the hydrological state variables in earth-rock dams, which in turn could facilitate the establishment of a theoretical basis for subsequent seepage inversion or hydrological-geophysical coupling analyses.

2 Methodology

2.1 Mathematical Description of Seepage Analysis

The unconfined seepage in an earth-rock dam is illustrated in Fig. 1. The problem domain is divided into two parts by the free surface AE. The part Ω_U above the free surface is the unsaturated region and the part Ω_S below the free surface is the saturated region, it is assumed that the seepage in the problem domain only flows through the saturated region.

In the saturated region of the dam, the water head at any point is mathematically expressed as (Darbandi et al. 2007):

$$h = \frac{p}{\rho g} + y \tag{1}$$

Fig. 1 Schematic diagram of unconfined seepage of dam
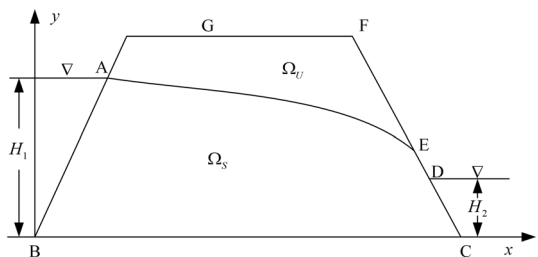
where h is the piezometric head of seepage, y is the vertical component coordinate, p, ρ and g are the fluid pressure, fluid density and gravity acceleration, respectively.

The equation of fluid continuity in the saturated domain is defined as (Bradet and Tobita 2002):

$$\nabla \cdot \mathbf{v} = 0 \tag{2}$$

According to Darcy's law, the seepage velocity in the saturated region is:

$$\mathbf{v} = \begin{pmatrix} v_x \\ v_y \end{pmatrix} = -\begin{pmatrix} k_x & k_{xy} \\ k_{xy} & k_y \end{pmatrix} \begin{pmatrix} \frac{\partial h}{\partial x} \\ \frac{\partial h}{\partial y} \end{pmatrix} \text{ or } \mathbf{v} = -\mathbf{k}\,\mathbf{grad}(h) \tag{3}$$

where k_x, k_y and k_{xy} are coefficients of the unit hydraulic conductivity $\mathbf{k}$, and v_x and v_y are the components of the discharge velocity vector $\mathbf{v}$. Hereafter we consider only the cases of isotropic permeability ($k_x = k_y$) and anisotropic permeability ($k_x \neq k_y$) that have the x- and y-axis for principal axes (i.e., $k_{xy} = 0$).

By substituting Eq. (3) into Eq. (2), the difference equation of two-dimensional unconfined steady seepage can be obtained:

$$\frac{\partial}{\partial x}\left(k_x \frac{\partial h}{\partial x}\right) + \frac{\partial}{\partial y}\left(k_y \frac{\partial h}{\partial y}\right) = 0 \tag{4}$$

As shown in Fig. 1, the corresponding boundary conditions are as follows:

1. Boundary conditions of AB and CD head of upstream and downstream reservoir water are:

$$h_{AB} = H_1 \tag{5}$$

$$h_{CD} = H_2 \tag{6}$$

2. The bottom boundary BC is impervious, which satisfies the discharge boundary conditions:

$$q_n = \mathbf{v} \cdot \mathbf{n} = 0 \tag{7}$$

where $\mathbf{n}$ is the upward normal unit vector. The flow rate in the upward normal direction is 0.

3. Free surface AE should satisfy two boundary conditions:

$$q_n = 0,\ h = y \tag{8}$$

4. Seepage surface DE satisfies boundary condition:

$$q_n \leq 0,\ h = y \tag{9}$$

2.2 S-FEM with Fixed Mesh

The whole problem domain is discretized by fixed grid of smoothed finite element, and the water head of each node can be obtained by interpolation:

$$u^h(\mathbf{x}) = \mathbf{NH} \tag{10}$$

where $\mathbf{N}$ is the shape function matrix and $\mathbf{H}$ is the water head of grid nodes. The head gradient needs to be obtained through solving the governing equation of unconfined seepage problem, and the shape function gradient needs to be calculated.

Smooth domains are typically divided by connecting the midpoints of relative line segments. Each smooth subdomain is composed of the field nodes, the smooth nodes at the center of edges and the Gaussian points. In an effort to seek the optimal balance between computational efficiency and accuracy, we specifically focus on the cases of SC = 1, 2, and 4 in this study, as illustrated in Fig. 2.

For the classical finite element methods, the gradient matrix of shape function can be generally obtained by solving the shape function derivation, while this gradient matrix of shape function can also be obtained by introducing the gradient smoothing technique into the methodology of our work:

$$\overline{\nabla}\mathbf{N}(\mathbf{x}) = \int_{\Omega_k^s} \nabla\mathbf{N}(\mathbf{x})\overline{W}(\mathbf{x}_k - \mathbf{x})\mathrm{d}\Omega \tag{11}$$

where $\overline{\nabla}\mathbf{N}(\mathbf{x})$ is the smooth shape function gradient, $\nabla\mathbf{N}(\mathbf{x})$ is the gradient of shape function, Ω_k^s is the smooth domain, and $\overline{W}(\mathbf{x}_k - \mathbf{x})$ is the smooth function (i.e., weight function).

The smooth function employed in our current work is a Heaviside-type function (Xue et al. 2013):

$$\overline{W}(\mathbf{x}_k - \mathbf{x}) = \begin{cases} \frac{1}{A_k^s}, \mathbf{x} \in \Omega_k^s \\ 0, \quad \mathbf{x} \notin \Omega_k^s \end{cases} \tag{12}$$
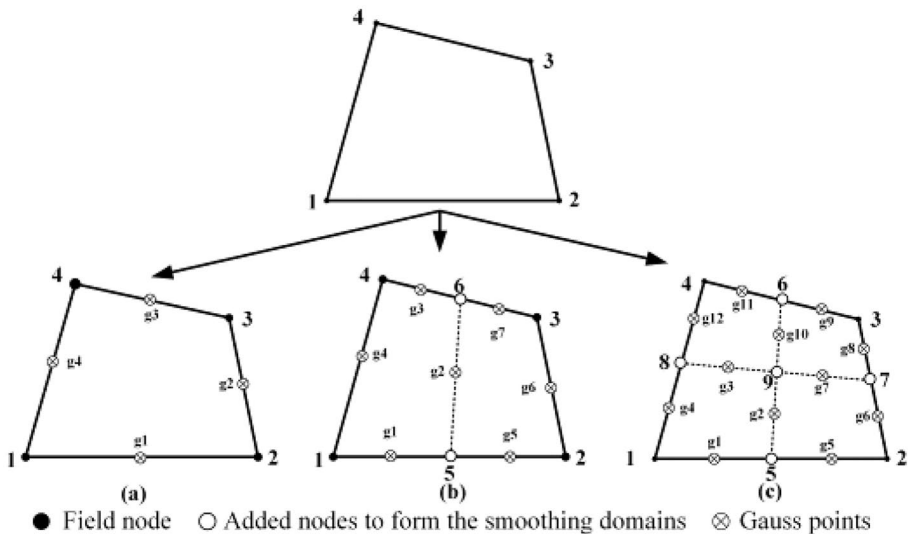
where A_k^s is the area of the smooth domain Ω_k^s.

Fig. 2 Division of element into the smoothing cells (SC): **a** SC = 1; **b** SC = 2; **c** SC = 4

The area integral can be transformed into the line integral by using uses integration by parts and then applies Gauss's divergence theorem, and Eq. (12) is then substituted into Eq. (11):

$$
\begin{aligned}
\overline{\nabla}\mathbf{N}(\mathbf{x}) &= \int_{\Omega_k^s} \nabla\mathbf{N}(\mathbf{x})\overline{W}(\mathbf{x}_k - \mathbf{x})\mathrm{d}\Omega \\
&= -\int_{\Omega_k^s} \mathbf{N}(\mathbf{x})\nabla\overline{W}(\mathbf{x}_k - \mathbf{x})\mathrm{d}\Omega + \frac{1}{A_k^s}\int_{\Gamma_k^s} \mathbf{N}(\mathbf{x})\mathbf{n}\mathrm{d}\Gamma \\
&= \frac{1}{A_k^s}\int_{\Gamma_k^s} \mathbf{N}(\mathbf{x})\mathbf{n}\mathrm{d}\Gamma
\end{aligned}
\tag{13}
$$

where Γ_k^s is the boundary of smooth domain Ω_k^s. $\mathbf{n}$ is the out of unit normal vector over Γ_k^s. It can be seen from Eq. (13) that the gradient smoothing technique converts the original two-dimensional area integral into a line integral along the boundaries.

By introducing Eq. (13) into Eq. (10), we obtain:

$$
\overline{\nabla}u^h(\mathbf{x}) = \overline{\mathbf{B}}\mathbf{H}
\tag{14}
$$

$$
\overline{\mathbf{B}} = \frac{1}{A_k^S}\int_{\Gamma_k^S} \mathbf{N}(\mathbf{x})\mathbf{n}\mathrm{d}\Gamma = [\, \overline{b}_x \ \overline{b}_y \,]
\tag{15}
$$

$$
\overline{b}_h = \frac{1}{A_k^S}\int_{\Gamma_k^s} \mathbf{N}(\mathbf{x})n_h(\mathbf{x})\mathrm{d}\Gamma, h = x, y
\tag{16}
$$

The smoothed matrix can be computed by using only the shape function values at mid-segment-points (Gauss points) on the each of segments within the smoothing domains. It is worthy of note that no derivatives of the shape functions are needed. The shape function values at each Gauss point are then calculated through linear interpolation using two end-points in the segment that contain these Gauss points (Liu and Trung 2016).

The governing equations and boundary conditions are then re-written into the integral weak form, and the water head interpolation is employed into the Galerkin weak form of the unconfined seepage problem:

$$
\overline{\mathbf{K}}\mathbf{H} = \mathbf{R}
\tag{17}
$$

where $\overline{\mathbf{K}}$ is the smooth stiffness matrix with the following form:

$$
\overline{\mathbf{K}} = \int_{\Omega} \overline{\mathbf{B}}^T \mathbf{k}\overline{\mathbf{B}}\mathrm{d}\Omega
\tag{18}
$$

where $\mathbf{k}$ is the matrix of unit hydraulic conductivity coefficient. In this weak form, $\mathbf{R}$ is related to the natural boundary conditions. According to the boundary conditions, the flowing along the outer normal direction of the boundary is 0, namely, $\mathbf{R} = \mathbf{0}$ (Kazemzadeh-Parsi and Daneshmand 2012).

When employing the fixed-grid method, the free surface divides the solution domain into two parts, generating three types of elements, as shown in Fig. 3. The element above the free surface is named as the external smooth element, the following element below free surface is named as the internal smooth element, and the element passing through the free surface is named as the intersecting smooth element.
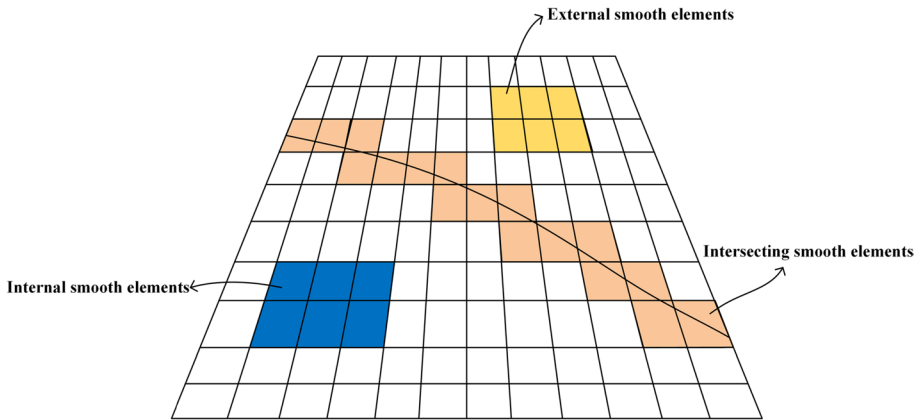
**Fig. 3** Schematic diagram of three types of smooth elements

The intersecting elements are separated by the free surface into different shapes, which shows a general *n*-polygon distribution (e.g., triangles or pentagons), as shown in Fig. 4. The greatest advantage of S-FEM lies in the convenience of direct integration along the element boundaries without having to consider the influence of element shape. Therefore, the element integral solution of *n*-polygon can refer to the quadrilateral case, and the Gaussian point function can be calculated by linear interpolation by using two endpoints of segment containing the Gauss point.

Hence, in our work, only the area below the free surface is considered, the influence of the stiffness matrix that formed by the external smooth elements above the free surface on the solution process is negligible. For the whole solution domain, the stiffness matrixes formed by both the internal smooth element and the intersecting smooth element are considered:

$$\overline{\mathbf{K}} = \int_{\Omega_1} \overline{\mathbf{B}}^T \mathbf{k}\overline{\mathbf{B}}\mathrm{d}\Omega + \int_{\Omega_2} \overline{\mathbf{B}}^T \mathbf{k}\overline{\mathbf{B}}\mathrm{d}\Omega \tag{19}$$

where Ω_1 is the internal smooth element region, Ω_2 is the intersecting smooth element region.

Fig. 4 Possible cases of boundary intersecting elements separated by the free surface
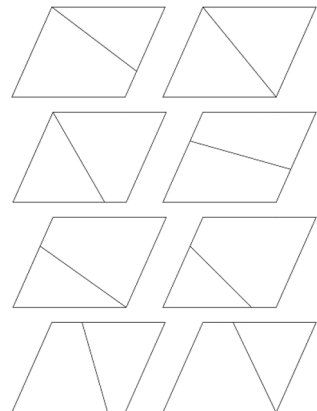
The Eq. (19) then can be re-written into the sum of elements integral:

$$\overline{\mathbf{K}} = \sum_{S1\in\Omega_1} \sum_S \int_{\Omega_S} \overline{\mathbf{B}}^T \mathbf{k} \overline{\mathbf{B}} d\Omega + \sum_{S2\in\Omega_2} \sum_S \int_{\Omega_S} \overline{\mathbf{B}}^T \mathbf{k} \overline{\mathbf{B}} d\Omega \tag{20}$$

where $S1$ is the smooth element belongs to Ω_1, $S2$ is the smooth element belongs to Ω_2.

In the calculation process, the permeability in each grid is constant, and the gradient matrix of smooth function is also a constant matrix, then the overall stiffness matrix is obtained:

$$\overline{\mathbf{K}} = \sum_{S1\in\Omega_1} \sum_S \left(A_S \overline{\mathbf{B}}_S^T \mathbf{k}_S \overline{\mathbf{B}}_S \right) + \sum_{S2\in\Omega_2} \sum_S \left(A_S \overline{\mathbf{B}}_S^T \mathbf{k}_S \overline{\mathbf{B}}_S \right) \tag{21}$$

where $\mathbf{k}_S$ is the permeability matrix at centroidal coordinate of the smoothing cell S.

By doing this, the proposed method is capable of optimizing the area integral calculated by the previous element stiffness matrixes into the line integral along the element boundaries with relatively high precision, which greatly simplifies the internal integration of those elements that intersect the boundaries. Compared to the conventional FEM, S-FEM alleviates difficulties in shape function calculations and precision loss caused by mesh shape distortion.

2.3 Iterative Updating Strategy

As demonstrated, the fundamental purpose of solving unconfined seepage problem is to find the dynamic position of free surface. According to the boundary conditions, the position and shape of the free surface are updated continuously in the iterations until a certain convergence condition is met. The framework of iteration is described as follows:

(i)   Select a line segment as the initial free surface, as shown in Fig. 5. The overflow point needs to be located on CE, while the initial point is located on BF.
(ii) On CE, a point D is selected as the initial solution of the overflow point of the free surface.
(iii) The line AD formed by connecting points A and D is used as the initial solution of the free surface.

Fig. 5 Schematic diagram of free surface update process
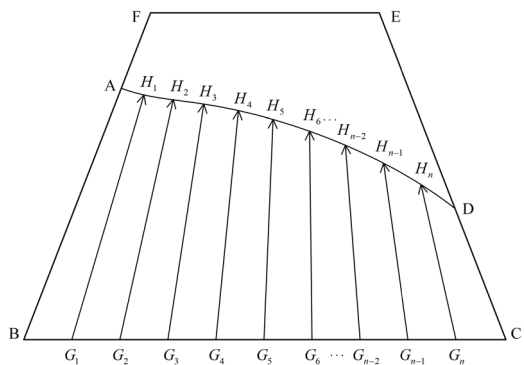
(iv) The initial free surface AD is cut into a series of control points H_1, H_2, …, H_n. Select a line segment such as BC as the baseline and divide the baseline BC into a series of base points G_1, G_2, …, G_n.

(v)   Connection points H_1 and G_1, points H_2 and G_2, and points H_n and G_n. A series of rays H_1G_1, H_2G_2, …, H_nG_n are obtained. In the iterative process, control points H_1, H_2, …, H_n to form the free surface, and then these control points move along these rays to constantly form a new free surface.

After completing the above preparatory work, the assumed initial free surface AD is utilized to solve Eq. (17), and the water head of each node in the solution domain can be obtained. The position of control points needs to be modified along the rays to satisfy the boundary conditions on the free surface.

The vertical coordinates of control points are:

$$y_i^{new} = y_i^{old} + \lambda\sigma_i \tag{22}$$

$$\sigma_i = h_i - y_i^{old} \tag{23}$$

where y_i^{old}, y_i^{new} are the elevation of the i-th key point in the previous iteration and the next iteration, respectively. h_i is the calculated piezometric head at the control point. λ is the step size to control the iteration speed, which is set as 0.8 in this study.

Before performing each iteration, the judgment is continuously performed to determine whether the following formula is satisfied:

$$\sigma = \frac{|\sigma_1| + |\sigma_2| + \ldots + |\sigma_n|}{n} < \varepsilon \tag{24}$$

$$Error = |\sigma_1| + |\sigma_2| + \ldots + |\sigma_n| \tag{25}$$

where ε is a small tolerance parameter (e.g., 10^{-2}).

Noting that once Eq. (24) is satisfied the iteration is terminated, otherwise, the control point positions are continuously updated according to Eq. (22).

It should be pointed out that under the control of the above updating strategy, since the overflow point is located on the right boundary of the dam model, and the head has been given in the boundary conditions, hence, the solution of overflow point is not suitable to update its location with the updating strategy, in turn, the locations of overflow point are determined by interpolating H_{n-1} and H_n in this study.

3 Verification Tests

The proposed algorithm is tested by solving the free surface of classical models for unconfined seepage problems, the novelty and computational efficiency of the algorithm is verified by comparing with the state-of-the-art techniques (Oden and Kikuchi 1980; Lacy and Prevost 1987; Bardet and Tobita 2002; Darbandi et al. 2007; Dai et al. 2019).

3.1 Rectangular Dam Model

Model 1 represents a standard and classical homogeneous rectangular dam, with a height of 10 m and a width of 5 m. The upstream water head is configured to be 10 m, while the downstream water head is set at 2 m. The permeability coefficient is set as 1 m/day, and the initial free surface is determined using the Dupuit formula (Dupuit 1863).

To highlight the specific features of different state-of-the-art methods, comparison results are presented in Fig. 6(a) to show the position of both the free surface and overflow point. As illustrated, the position of the free surface calculated by the proposed method has a good coincidence with the measurement data obtained by other methods, which preliminarily verified that the proposed method suitably predicts the position of the free surface, as well as the overflow point. It can also be found that the division manner of different smooth domains has little influence on the results of the free surface.

In addition, the contour map of water head, velocity vector distribution and fluid pressure are imaged in Fig. 6(b)–(d), which also implies that the zero-pressure contour result is well consistent with the free surface. Herein the forward region is divided into 450 units and 496 nodes. All simulation tests were performed on the desktop of Dell 8930 with Intel(R) Core TM i7-8700 @3.70 GHz and with the physical memory of 64.0 GB under Window 10 operating system.

The convergence performance of the proposed method in this study is documented and presented in Fig. 7. The results show that the global convergence is consistently and favorably improving throughout the entire iterative process. Notably, this global convergence stands in stark contrast to techniques that rely on moving grids (Darbandi et al. 2007; Dai et al. 2019). The total number of iterations count for SC=1, SC=2, and SC=4 is 9, 9, and 20, respectively. The corresponding running times are 0.43 s, 0.55 s, and 1.18 s, respectively.

In fact, the rate of flow quantity through distinct vertical sections in the dam should be theoretically equal by following (Zheng et al. 2015):

$$Q(x) \; = \; \int_0^{y_F} v_x \mathrm{d}y = \text{constant} \tag{26}$$
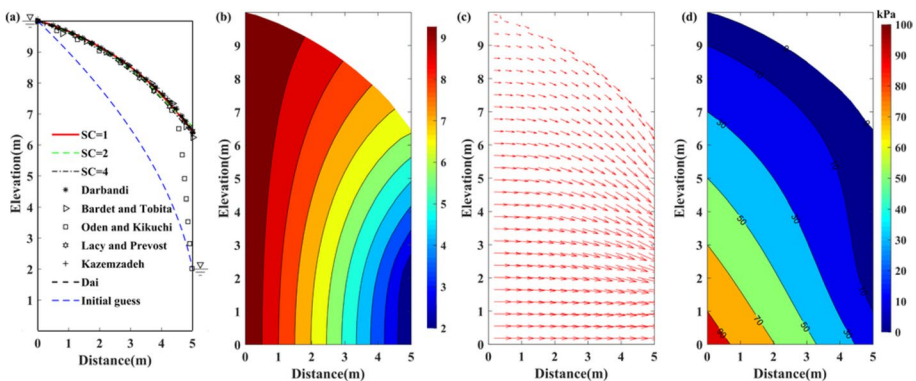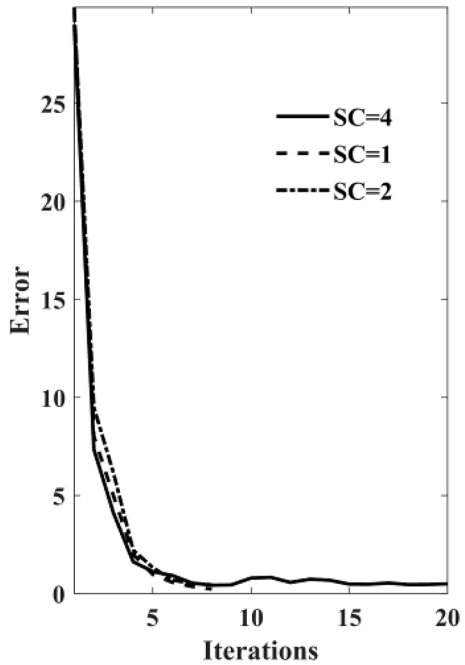
where y_F is the ordinate of free surface.

Fig. 6 Results of homogeneous rectangular dam **a** Comparison of the free surface assessed from available results. **b** Contour map of water head. **c** Distribution of velocity vector. **d** Contour map of fluid pressure

Fig. 7 Convergence behavior
of the proposed method for the
homogeneous rectangular dam

The distribution of flow quantities along the *x*-axis in the proposed method is documented and illustrated in Fig. 8. It's evident that the flow rates across different vertical sections are almost uniform, and the presence of different smooth domains has a minimal impact on the computational outcomes.
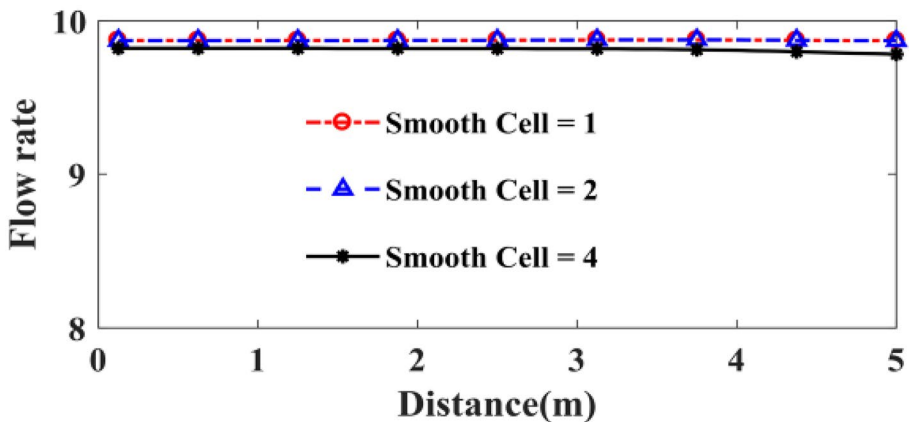

Fig. 8 Flow quantity distribution through the different vertical segments along the *x* axis

3.2 Rectangular Dam Model with Interface

The model 2, initially introduced by Oden & Kikuchi (1980), has become a standard benchmark for evaluating the accuracy of various numerical methods. This model consists of a rectangular dam with an interface located at its midpoint. It's worth noting that the permeability coefficient is 1 m/day on the left side and 10 m/day on the right. The upstream and downstream water head remains the same as in the previous model.

The initial free surface is still determined using the Dupuit formula. Figure 9(a) displays the comparative outcomes of free surface determination using various numerical techniques for this classic model. The contour map of water head, velocity vector distribution, and fluid pressure for this model is presented in Fig. 9(b)–(d). It demonstrates that in regions with low permeability, seepage velocity is relatively slow, and water head variations are minimal, resulting in a dense contour distribution. Conversely, in areas with high permeability, seepage velocity is higher, water head changes dramatically, and the contour distribution is relatively sparse. Significant fluid pressure changes can be observed, particularly at the boundaries of different permeability zones.

3.3 Right-Angle Trapezoidal Dam Model

The model 3 is constructed as a right-angled trapezoidal dam with a base width of 7 m and top width of 2 m. The upstream water head is set at 5 m, while the downstream water head is set at 1 m, and the permeability coefficient is set as 1 m/day.

As depicted in Fig. 10(a), a structured-grid scheme has been employed for calculating the free surface within this third classical model. The results obtained through our GST-based S-FEM exhibit strong concordance with those from other methodologies, as demonstrated in Fig. 10(b). Figure 10(c)–(e) display the contour maps of water head, velocity vector distribution, and fluid pressure for this model. Figure 10(c) reveals that water head contour lines intersect the free surface perpendicularly. Figure 10(d) illustrates that in the vicinity of the free surface, the seepage velocity is aligned parallel to it, directed towards the overflow point, while maintaining a zero outer normal velocity,
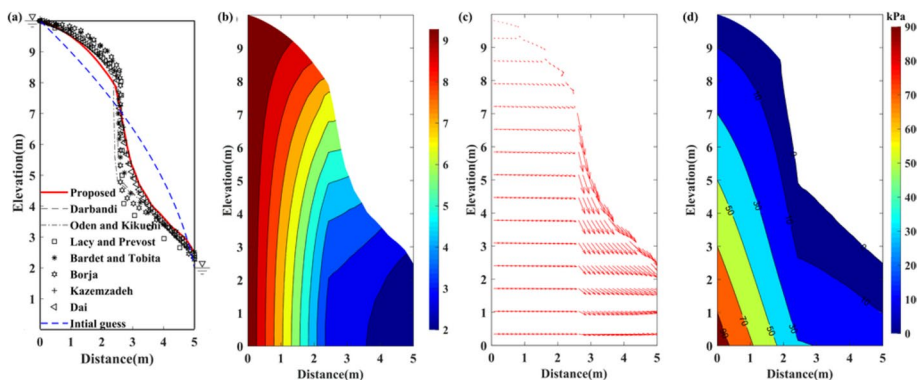

Fig. 9 Results of rectangular dam model with interface **a** Comparison of the free surface assessed from available results. **b** Contour map of water head. **c** Distribution of velocity vector. **d** Contour map of fluid pressure
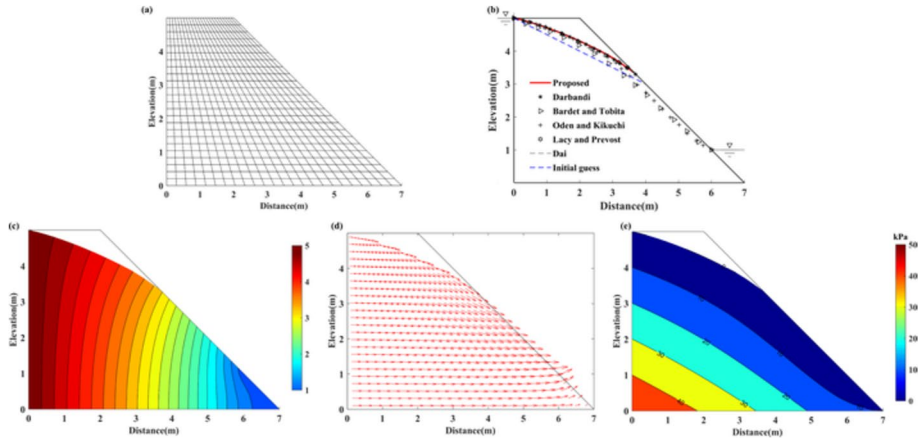
Fig. 10 Results of right-angle trapezoidal dam model **a** Schematic diagram of meshing. **b** Comparison of the free surface assessed from available results. **c** Contour map of water head. **d** Distribution of velocity vector. **e** Contour map of fluid pressure

consistent with the free surface boundary condition outlined in Eq. (8). Additionally, the zero-pressure lines consistently coincide with the free surface, as shown in Fig. 10(e).

3.4 Isosceles Trapezoidal Dam Model

The model 4 is designed as an isosceles trapezoidal dam with a top side length of 4 m, a bottom side length of 14 m, and a height of 6 m. The upstream water head and the downstream water head are set as 5 m and 1 m, respectively. The permeability coefficient within the solution domain is maintained at 1 m/day.
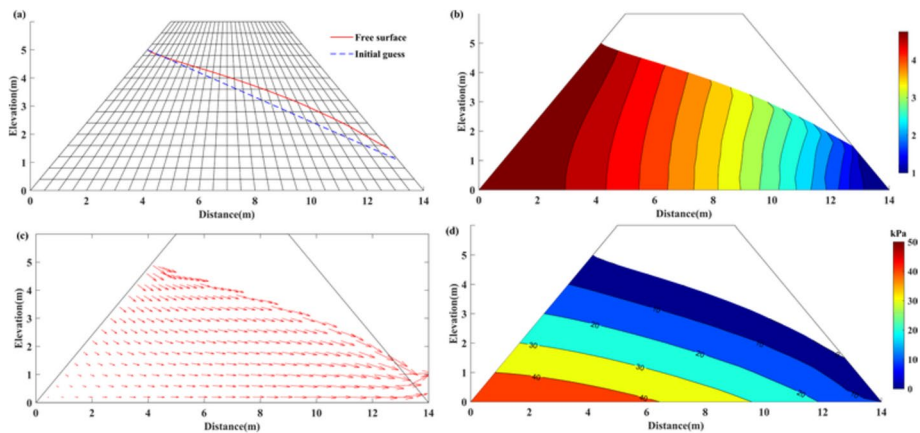
Fig. 11 Results of Isosceles trapezoidal dam model **a** Schematic diagram of meshing and comparison of the free surface with initial free surface. **b** Contour map of water head. **c** Distribution of velocity vector. **d** Contour map of fluid pressure

Figure 11(a) illustrates the schematic diagram of meshing and a comparison of the free surface against the initial free surface. Figure 11(b)–(d) display the contour maps of water head, velocity vector distribution, and the fluid pressure for this model. The outcomes are similar to those of model 3.

In earth-rock dams, the position of free surface is always affected by different permeability of rock blocks to varying degrees (Lacy and Prevost 1987). Namely, ignoring the influence of permeability anomalies may leads to a biased free surface searching result especially in real applications, which regarding both the accurate shape and exact position of free surface. More importantly, permeability anomalies interpretation based on the searching results is also a significant part of the multi-parameters seepage inversion regarding water head, free surface solution, overflow point, seepage velocity and fluid pressure. Within this context and for the first attempt, we further explored these specific impacts in an effort to improve the accuracy and practicability of multi-parameter seepage inversion.

4 Exploratory Tests

4.1 Rectangular Dam Model with a Single Anomaly

The first exploratory tests model introduces different permeability anomalies of low or high permeability into the model 1. To emphasize the effect of anomaly placement on the free surface, two distinct models with different anomaly positions are created, denoted as Example 1 and Example 2. The coordinates of the anomaly in Example 1 and Example 2 are [2, 8.43; 3, 8.43; 3, 7.7; 2, 7.7], [1, 2.2; 2, 2.2; 2, 1.1; 1, 1.1], respectively. These models are illustrated in Fig. 12(a) and (b). The black dotted box delineates the area of the anomaly. The permeability of background area is set as 1 m/day. Four distinct permeability anomalies, namely cases 1 to 4, are detailed in Table 1. Boundary conditions and model meshing remain consistent with those of the rectangular dam model in Section 3.1.

Figure 12(a) demonstrates the impact on the free surface when the anomaly is located in close proximity to the free surface. Interestingly, when the permeability of the anomaly surpasses that of the background medium, the free surface curve tends to bend towards the anomaly. Conversely, when the permeability of the anomaly is lower than that of the background medium, the free surface curve bends away from the anomaly. The degree of influence becomes more pronounced as the contrast between anomaly and background permeabilities increases. Figure 12(b) illustrates that when the anomaly is located at a significant distance from the free surface, its influence on the free surface diminishes. However, as shown in Table 1, the position of the overflow point is affected by the anomaly, whether it is positioned near or far from the free surface.

Figures 13 and 14 depict the alterations in seepage velocity distribution caused by various permeability anomalies. These figures reveal that, as abnormal permeability gradually transitions from values lower than the background permeability to higher values, seepage velocity within the anomalous region notably increases. The shift in flow direction evolves from repulsion (primarily attributed to low permeability anomalies) to aggregation (primarily induced by the presence of high permeability anomalies).

Comparing the results between Example 1 and 2, one can find that when the anomaly is situated in close proximity to the free surface, its influence on seepage velocity is relatively limited. This can be attributed to the relatively low seepage velocity
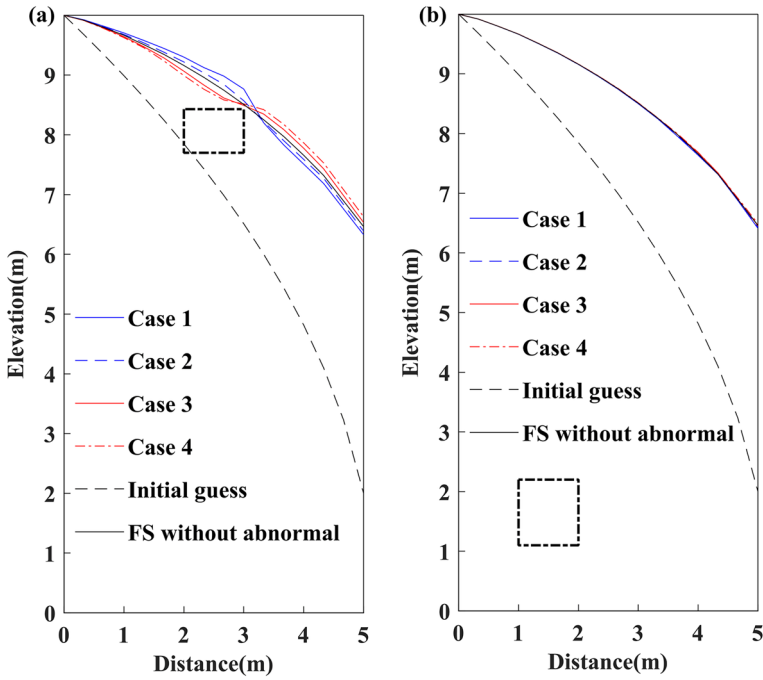
Fig. 12 Location of the anomaly and the free surface result **a** Example 1. **b** Example 2

magnitude in the immediate vicinity of the free surface, while its effect on the free surface is more pronounced. Conversely, when the anomaly is located far away from the free surface, its position has a more pronounced effect on the seepage velocity, with a lesser effect on the free surface.

4.2 Rectangular Dam Model with Multiple Anomalies

The second exploratory test model aims to investigate the specific effects of multiple anomalies on hydrologic state variable, encompassing water head, flow velocity, and fluid pressure. The positions of three anomalies are illustrated in Fig. 15, with the red dotted box indicating high permeability ($k = 10$ m/day) and the blue dotted box representing low permeability ($k = 0.1$ m/day). The coordinates of the three anomalies are [1, 1.97; 1.67, 1.97;

Table 1 Overflow point position (Examples 1 and 2) for different cases of permeability considered in the rectangle dam

| Case number	Permeability (meter/day)	Overflow point position /m	
		Example 1	Example 2
Case 1	0.1	6.3288	6.4116
Case 2	0.5	6.3896	6.4369
Case 3	3.0	6.5334	6.4537
Case 4	10.0	6.6301	6.4884
Background	1.0	6.4635	6.4635
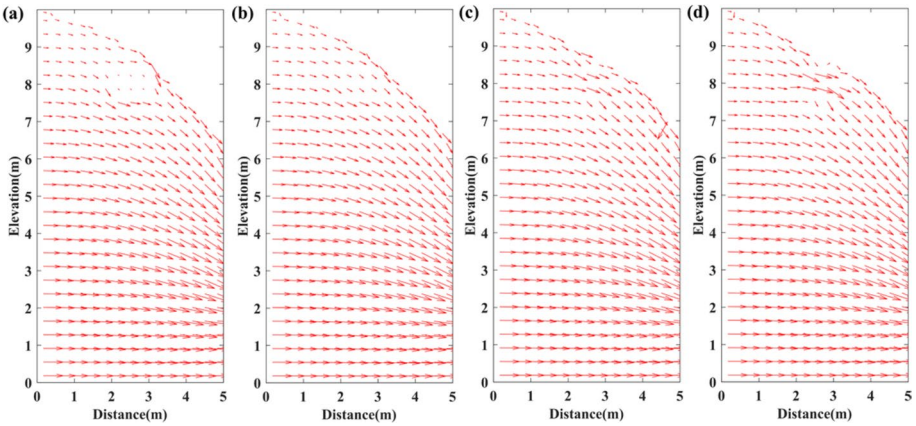
Fig. 13 Comparison of seepage velocity for different cases of permeability in the rectangle dam (Example 1): **a** Case 1, $k=0.1$ m/day; **b** Case 2, $k=0.5$ m/day; **c** Case 3, $k=3$ m/day; **d** Case 4, $k=10$ m/day

1.67, 8.43; 1, 8.43], [2.33, 6.97; 3.33, 6.97; 3.33, 6.23; 2.33, 6.23], [1, 2.2; 2, 2.2; 2, 1.1; 1, 1.1], respectively. The permeability of background area is set as 1 m/day. Boundary conditions and model meshing remain consistent with those of the model 1 in Section 3.1.

As depicted in Fig. 15(a) and (c), the trends in free surface and seepage velocity variations in the multi-anomaly model closely resemble those observed in the single-anomaly model. Figure 15(b) and (d) demonstrate that, due to the attractive properties, the existence of high permeability anomalies significantly increases the seepage velocity in the high permeability area. This leads to a sparser distribution of water head and fluid pressure contours. Conversely, the existence of low permeability anomalies, which may have a repulsive effect on seepage, results in a significant decrease in seepage velocity within the low permeability area, causing a denser distribution of water head and fluid pressure contours.
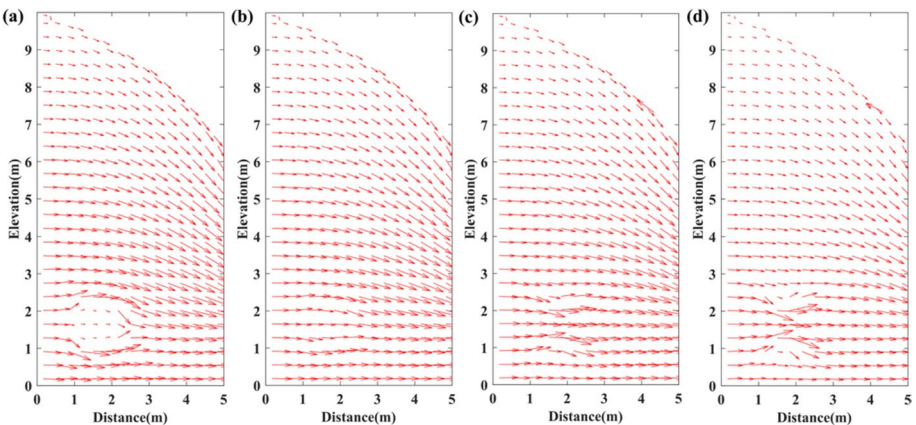
Fig. 14 Comparison of seepage velocity for different cases of permeability in the rectangle dam (Example 2): **a** Case 1, $k=0.1$ m/day; **b** Case 2, $k=0.5$ m/day; **c** Case 3, $k=3$ m/day; **d** Case 4, $k=10$ m/day
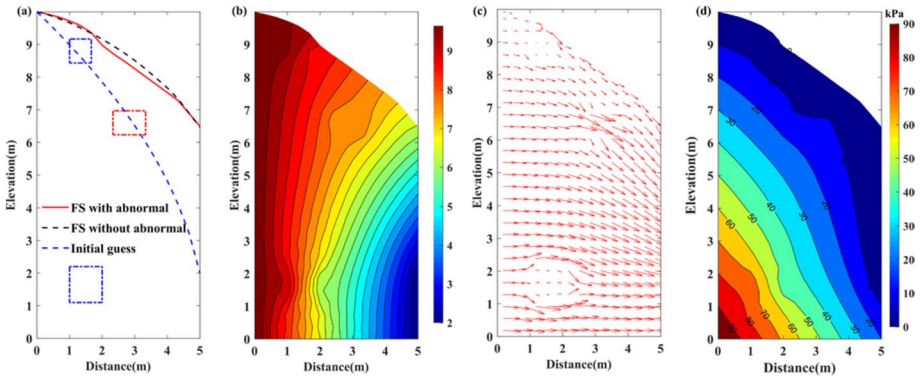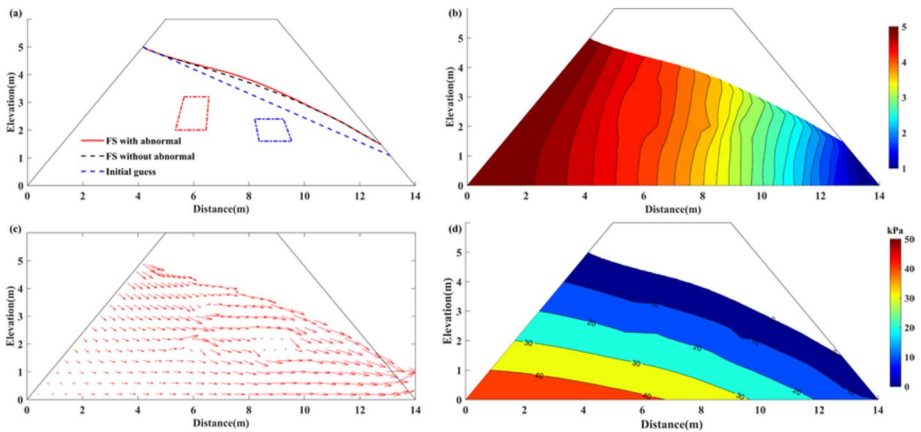
Fig. 15 Rectangle dam with multiple anomalies **a** Schematic diagram of model and free surface result. **b** Contour map of water head. **c** Distribution of velocity vector. **d** Contour map of fluid pressure
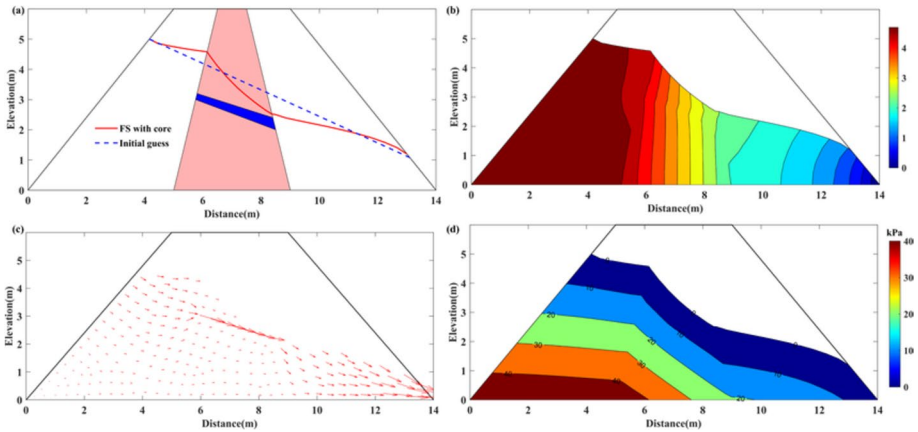
4.3 Trapezoidal Dam Model with Anomalies

The third model features an isosceles trapezoidal dam with two distinct permeability anomalies, as depicted in Fig. 16(a). The red dotted box corresponds to a high permeability anomaly ($k = 10$ m/day), while the blue dotted box represents a low permeability anomaly ($k = 0.1$ m/day). The coordinates of the two anomalies are [5.66, 3.2; 6.55, 3.2; 6.44, 2; 5.43, 2], [8.2, 2.4; 9.24, 2.4; 9.54, 1.6; 8.37, 1.6], respectively. The permeability of background area is set as 1 m/day. Boundary conditions and model meshing remain consistent with those of the trapezoid dam model in Section 3.4.

Figure 16 (a) depicts the model diagram and free surface outcomes. Figure 16(b)–(d) illustrate the distribution of water head, seepage velocity, and fluid pressure, respectively. It is evident that in trapezoidal dams, high and low permeability anomalies have a consistent impact on water head, seepage velocity, and fluid pressure.

Fig. 16 Trapezoidal dam model with anomalies **a** Schematic diagram of model and free surface result. **b** Contour map of water head. **c** Distribution of velocity vector. **d** Contour map of fluid pressure

Fig. 17 Trapezoidal dam model with core wall and leakage path **a** Schematic diagram of model and free surface result. **b** Contour map of water head. **c** Distribution of velocity vector. **d** Contour map of fluid pressure

4.4 Trapezoidal Dam Model with Core Wall and Leakage Path

Finally, to evaluate the method's performance and practicality in complex model applications, we investigate a common scenario of dam seepage failure. As shown in Fig. 17(a), we constructed a model of an isosceles trapezoidal earth-rock dam with a core wall and thoughtfully designed leakage path through the core wall. The coordinates of the core wall are [6.5, 6; 7.5, 6; 9, 0; 5, 0], and the coordinates of the leakage path are [5.8, 3.2; 8.4, 2.4; 8.5, 2; 5.75, 3]. This specially designed model could reveal the common seepage features of the in-site dams. The permeability of core wall and leakage passageway are set as 0.1 m/day, 1 m/day, respectively.

Figure 17(a) presents the free surface results. It can be found that there are two distinct inflection points on the free surface at the interface between the core wall and the dam. As observed in Fig. 17(c), the flow velocity within the low-permeability core wall significantly decreases, while the velocity within the leakage pathway exhibits an apparent increase, indicating a trend of concentrated seepage towards the leakage pathway. In Fig. 17(b) and (d), the contour distributions of water head and fluid pressure follow the patterns that similar to those discussed earlier.

5 Discussion

The experimental findings demonstrate that the SFEM can be utilized not only for saturated seepage problems but also for more complicated seepage scenarios. This could provide a viable option for addressing the computational efficiency and accuracy challenges in free surface search. For instance, in intricate three-dimensional seepage problems, GTS' characteristics enable the reduction of dimensional integrals. By doing this, computational complexity can be reduced while ensuring the accuracy of solutions. More importantly, conducting multi-parameter seepage inversion is made possible by relevant findings on the impact of seepage anomalies and the dam's auxiliary structures on hydrological state variables. Furthermore, it could serve as constraints for hydro-geophysical inversion, which will be the focus of our future work.

6 Conclusions

In this paper, we employed the S-FEM to accurately solve the free surface of unconfined seepage fields in both homogeneous and heterogeneous earth-rock dams. A thorough analysis is conducted to determine a suitable balance between efficiency and accuracy regarding the impact of SC on the solution. The feasibility and effectiveness of the proposed method are validated by comparisons with the results of classical models in references.

A potential contribution of this work is the comprehensive consideration of specific interactions between the location of anomalies and the magnitude of permeability on hydrological state variables, including the overflow point, seepage velocity, and fluid pressure. This analysis represents an impact exploration that could provide insights into the coupled and combined effects of anomaly characteristics on various hydrological parameters. More importantly, the proposed methodology improves the capacity to maintain high accuracy of the solution with a preferable search efficiency in handling the complicated cases of heterogeneous dam applications. The commercialization of precise dimension detecting of leakage anomalies within the heterogeneous earth dam could be facilitated by this contribution.

Availability of Data and Materials Available upon reasonable request.

Declarations

References

Bardet JP, Tobita T (2002) A practical method for solving free-surface seepage problems. Comput Geotech 29(6):451–475. https://doi.org/10.1016/S0266-352X(02)00003-4

Bazyar MH, Talebi A (2015) Transient seepage analysis in zoned anisotropic soils based on the scaled boundary finite-element method. Int J Numer Anal Met 39(1):1–22

Butera I, Climaci M, Tanda MG (2020) Numerical analysis of phreatic levels in river embankments due to flood events. J Hydrol 590:125382. https://doi.org/10.1016/j.jhydrol.2020.125382

Dai Q, Lei Y, Zhang B, Feng D, Wang X, Yin X (2019) A practical adaptive moving-mesh algorithm for solving unconfined seepage problem with Galerkin finite element method. Sci Rep 9(1):1–15. https://doi.org/10.1038/s41598-019-43391-4

Daneshmand F, Kazemzadeh-Parsi MJ (2009) Static and dynamic analysis of 2D and 3D elastic solids using the modified FGFEM. Finite Elem Anal Des 45(11):755–765. https://doi.org/10.1016/j.finel.2009.06.003

Darbandi M, Torabi SO, Saadat M, Daghighi Y, Jarrahbashi D (2007) A moving-mesh finite-volume method to solve free-surface seepage problem in arbitrary geometries. Int J Numer Anal Met 31(14):1609–1629. https://doi.org/10.1002/nag.611

Desai CS, Li GC (1983) A residual flow procedure and application for free surface flow in porous media. Adv Water Resour 6(1):27–35. https://doi.org/10.1016/0309-1708(83)90076-3

Dou Z, Wu J, Zhang H, Huang K (2017, June) The solution of unconfined water seepage problem in saturated-unsaturated soil using Bathe algorithm and Signorini condition. IOP Conf Sers: Earth Environ Sci 69(1):012170. IOP Publishing

Dupuit JE (1863) Etudes théoriques et pratiques sur le mouvement des eaux dans les canaux découverts et à travers les terrains perméables avec des considérations relatives au régime des grandes eaux, au débouché à leur donner, et à la marche des des alluvions dans les rivières à fond mobile. 2éme édition, Dunod, éditeur, Paris

Farzin S, Meysam N, John A (2020) Upstream cutoff and downstream filters to control of seepage in dams. Water Resour Manag 34:4271–4288. https://doi.org/10.1007/s11269-020-02674-6

He ZC, Liu GR, Zhong ZH, Zhang GY, Cheng AG (2011) A coupled ES-FEM/BEM method for fluid-structure interaction problems. Eng Anal Bound Elem 35(1):140–147

Johari A, Heydari A (2018) Reliability analysis of seepage using an applicable procedure based on stochastic scaled boundary finite element method. Eng Anal Bound Elem 94:44–59. https://doi.org/10.1016/j.enganabound.2018.05.015

Jiang QH, Deng SS, Zhou CB, Lu WB (2010) Modeling unconfined seepage flow using three-dimensional numerical manifold method. J Hydrodyn 22(4):554–561. https://doi.org/10.1016/S1001-6058(09)60088-3

Lacy SJ, Prevost JH (1987) Flow through porous media: a procedure for locating the free surface. Int J Numer Anal Met 11(6):585–601. https://doi.org/10.1002/nag.1610110605

Liu GR, Dai KY, Nguyen TT (2007) A smoothed finite element method for mechanics problems. Comput Mech 39(6):859–877. https://doi.org/10.1007/s00466-006-0075-4

Liu GR, Trung N (2016) Smoothed finite element methods. CRC Press. https://doi.org/10.1201/EBK1439820278

Liu GR, Nguyen-Thoi T, Lam KY (2009) An edge-based smoothed finite element method (ES-FEM) for static, free and forced vibration analyses of solids. J Sound Vib 320(4–5):1100–1130. https://doi.org/10.1016/j.jsv.2008.08.027

Nafiseh K, Mehdi V, Mohammad RN, Somayeh PR (2018) Multi-objective hydraulic optimization of diversion dam's cut-off. Water Resour Manag 32:3723–3736. https://doi.org/10.1007/s11269-018-2015-4

Kazemzadeh-Parsi MJ, Daneshmand F (2012) Unconfined seepage analysis in earth dams using smoothed fixed grid finite element method. Int J Numer Anal Met 36(6):780–797. https://doi.org/10.1002/nag.1029

Kazemzadeh-Parsi MJ, Daneshmand F (2013) Three dimensional smoothed fixed grid finite element method for the solution of unconfined seepage problems. Finite Elem Anal Des 64:24–35. https://doi.org/10.1016/j.finel.2012.09.001

Oden JT, Kikuchi N (1980) Theory of variational inequalities with applications to problems of flow through porous media. Int J Eng Sci 18(10):1173–1284

Rehamnia I, Benlaoukli B, Heddam S (2020) Modeling of seepage flow through concrete face rockfill and embankment dams using three heuristic artificial intelligence approaches: a comparative study. Environ Process 7(1):367–381. https://doi.org/10.1007/s40710-019-00414-6

Shahrokhabadi S, Toufigh MM (2013) The solution of unconfined seepage problem using Natural Element Method (NEM) coupled with Genetic Algorithm (GA). Appl Math Model 37(5):2775–2786. https://doi.org/10.1016/j.apm.2012.06.030

Sharma V, Fujisawa K, Murakami A (2021) Space-time finite element method for transient and unconfined seepage flow analysis. Finite Elem Anal Des 197:103632

Xue BY, Wu SC, Zhang WH, Liu GR (2013) A smoothed FEM (S-FEM) for heat transfer problems. Int J Comp Meth 10(01):1340001. https://doi.org/10.1142/S021987621340001X

Yang Y, Sun G, Zheng H (2019) Modeling unconfined seepage flow in soil-rock mixtures using the numerical manifold method. Eng Anal Bound Elem 108:60–70

Zhang W, Dai B, Liu Z, Zhou C (2017) Unconfined seepage analysis using moving kriging mesh-free method with Monte Carlo integration. Transport Porous Med 116(1):163–180. https://doi.org/10.1007/s11242-016-0769-9

Zheng H, Liu DF, Lee CF, Tham LG (2005) A new formulation of Signorini's type for seepage problems with free surfaces. Int J Numer Meth Eng 64(1):1–16. https://doi.org/10.1002/nme.1345

Zheng H, Liu F, Li C (2015) Primal mixed solution to unconfined seepage flow in porous media with numerical manifold method. Appl Math Model 39(2):794–808. https://doi.org/10.1016/j.apm.2014.07.007